Journal of Computational Physics **159,** 425–439 (2000)
doi:10.1006/jcph.2000.6455, available online at http://www.idealibrary.com on IDEAL®

Two- and Three-Dimensional Nonlocal Density Functional Theory for Inhomogeneous Fluids

II. Solvated Polymers as a Benchmark Problem

Laura J. Douglas Frink*,[1] and Andrew G. Salinger†

*Computational Biology and Materials Technology Department and †Parallel Computational Sciences Department, Sandia National Laboratories, Albuquerque, New Mexico 87185
E-mail: *ljfrink@sandia.gov, †agsalin@sandia.gov

Received August 23, 1999; revised January 19, 2000

In a previous companion paper, we presented the details of our algorithms for performing nonlocal density functional theory calculations in complex two- and three-dimensional geometries. We discussed scaling and parallelization, but did not discuss other issues of performance. In this paper, we detail the precision of our methods with respect to changes in the mesh spacing. This is a complex issue because given a Cartesian mesh, changes in mesh spacing will result in changes in surface geometry. We discuss these issues using a series of rigid solvated polymer models including square rod polymers, cylindrical polymers, and bead–chain polymers. In comparing the results of the various models, it becomes clear that surface curvature or roughness plays an important role in determining the strength of structural solvation forces between interacting solvated polymers. The results in this paper serve as benchmarks for future application of these algorithms to complex fluid systems.

Key Words: density functional theory; solvation force; colloidal stability; DNA; polymer; liquid crystals.

1. INTRODUCTION

Fluids near surfaces or macromolecules have properties (viscosity, density, etc.) that differ significantly from the bulk properties of these fluids. Predicting the structure of fluids in confined spaces is ultimately critical for understanding adsorption in [1], solvation forces on [2, 3], and wetting [4] of complex surfaces [5, 6], macromolecules, and porous materials [7].

[1] To whom correspondence should be addressed.

0021-9991/00 $35.00

In Part I of this series [8], details of a novel numerical implementation of an accurate nonlocal density functional theory (DFT) were presented. These algorithms have enabled calculation of density distributions of fluids near complex surfaces that require two-dimensional (2D) or 3D solutions. In this paper, we focus on the precision of the calculations using solvated polymers to motivate the discussion. Calculations based on several models are presented to address a variety of numerical issues that may affect the results. These issues include mesh refinement and precision, internal consistency (sum rules), and geometry change with mesh refinement. These issues are addressed in detail in Sections 3 and 4 using 2D polymer models. In Section 5, the results from 3D calculations are presented.

The particular nonlocal DFT we apply was detailed in Part I. Briefly, the DFT is based on the functional minimization of the grand free energy, Ω, with respect to the density distributions, $\rho(\mathbf{r})$, at constant temperature, T, and fluid chemical potential, μ [9]:

$$\left(\frac{\delta\Omega}{\delta\rho(\mathbf{r})}\right)_{T,\mu} = 0. \tag{1}$$

The particular free energy functional, $\Omega[\bar{\rho}(\mathbf{r})]$ we use was developed by Rosenfeld [10].

The principle outputs of the DFT calculation are the surface free energy, Ω^s, the solvation force, $\mathbf{f}$, and the excess adsorption, Γ. Boldface indicates a vector with $\mathbf{f} \equiv (f^x, f^y, f^z)$. These parameters are defined and calculated via

$$\Omega^s = \Omega[\rho(\mathbf{r})] - \Omega[\rho_b], \tag{2}$$

$$\mathbf{f}_s = \int \rho(\mathbf{r_s})\mathbf{n}\, d\mathbf{r_s}, \tag{3}$$

and

$$\Gamma = \int [\rho(\mathbf{r}) - \rho_b]\, d\mathbf{r}, \tag{4}$$

where ρ_b is the bulk fluid density associated with the known μ, $\int d\mathbf{r_s}$ indicates a surface integral, $\mathbf{n}$ is the unit normal to the surface, and $\int d\mathbf{r}$ indicates a volume integral. The net force on a given surface is found by integrating over the fluid densities in contact with the surface (Eq. (3)). Since the integral is taken over the entire surface, the solvation force is strictly zero when a surface is isolated in solution or when two surfaces are far apart. It should be noted that the solvation force as expressed in Eq. (3) has already been specialized to the hard potential systems we consider in this paper.

One way to test the precision of the calculations is to test the self-consistency of the solutions via sum rules [9]. While there are a variety of sum rules that apply to inhomogeneous fluids, the one we consider here is the force sum rule. Assuming that the line of centers between two surface lies in the x-direction, the force in this direction is

$$f_s^x = \int \rho(\mathbf{r_s}) n_x\, d\mathbf{r_s} = -\frac{\partial\Omega^s}{\partial D}, \tag{5}$$

where D is the separation between the two surfaces.

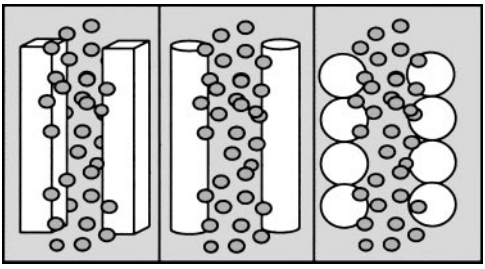

FIG. 1. A schematic of the three solvated polymer models of interest. Square rod polymers are shown on the left, cylindrical polymers are shown in the center, and bead–chain polymers are shown on the right.

2. POLYMER MODELS

As in Part I we restrict the current discussion to hard sphere fluids in contact with hard surfaces. In the cases we discuss here, the surfaces are designed to model rigid polymers. More specifically, the surfaces are small in two dimensions, but long and regular in the third. The stiffness of these models is not a realistic representation of many polymers, but there are some important exceptions. One example is deoxyribonucleic acid (DNA). The double helix of the DNA causes this important polymer to be quite rigid. As a result, DNA has often been treated from a modeling point of view as a rigid polymer [11, 12].

The specific models we present here are square rod polymers, cylindrical polymers, and bead–chain polymers. The three types of models are sketched in Fig. 1. While the solvation of square rod and cylindrical polymer models may be studied in 2D, the bead–chain polymer requires a 3D calculation. Sketches of the 2D and 3D computational domains are shown in Fig. 2. In the 2D cases, boundaries at both $x = L_x$ and $y = L_y$ are reflective (see Part I for a precise definition). In the 3D calculations the $y = L_y$, $z = 0$, and $z = L_z$ boundaries are reflective. All remaining boundaries assume that the fluid surrounding the computational domain has $\rho = \rho_b$. Given the reflective boundaries, the computational domain is clearly one quarter of the relevant physical domain, and the physical domain is composed of two polymer strands suspended in the hard sphere fluid.

3. SQUARE ROD POLYMERS

In Part I, we outlined a variety of numerical algorithms for solving the Euler–Lagrange equations of the DFT. We showed how such algorithms perform as a function of total domain size and mesh spacing on a Cartesian mesh. However, we did not discuss issues of precision. In this section we present sensitivity studies and self-consistency tests with respect to mesh spacing for the square rod polymer. This model is unique in that the geometry of the polymer is invariant with respect to changes in mesh spacing. One example of the density distribution in the solvation shell around two square rod polymers is shown in Fig. 3, where the surface separation is $D/\sigma = 1.5$. In all that follows, the mesh spacing is denoted Δx with the understanding that this mesh spacing corresponds to the mesh zone adjacent to the polymer surface (see Part I for a description of the mesh coarsening).

The surface free energy, the x-component of the solvation force, and the excess adsorption are shown in Fig. 4, as a function of both the surface separation of two polymer strands and the mesh spacing. In all cases, Δx varies from 0.25σ to 0.025σ, where σ is the fluid

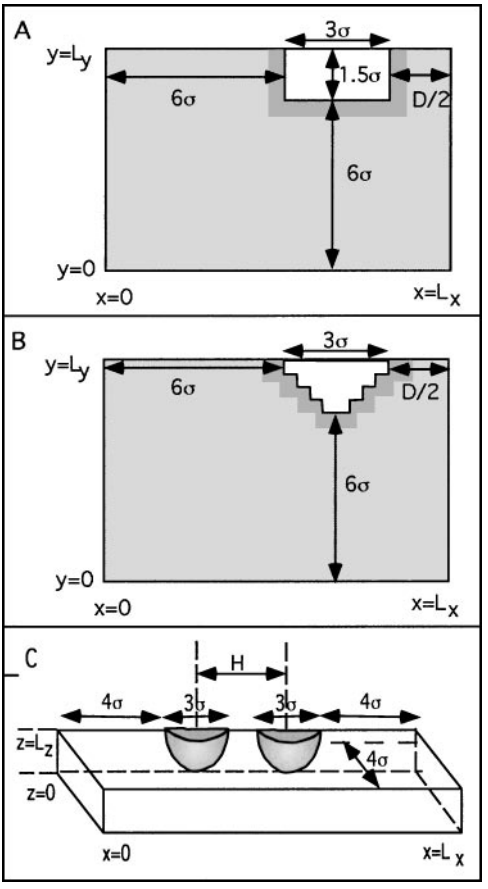

FIG. 2. Sketches of the computational domains used for (A) the 2D square-rod polymer, (B) the 2D cylindrical polymer, and (C) the 3D bead–chain polymer calculations. The minimum surface separation is indicated by D while the center–center separation is indicated by H. The shaded regions in (A) and (B) indicate exclusion zones of width 0.5σ, where no fluid is found due to hard core repulsions. The exclusion zones are omitted from (C) for clarity.

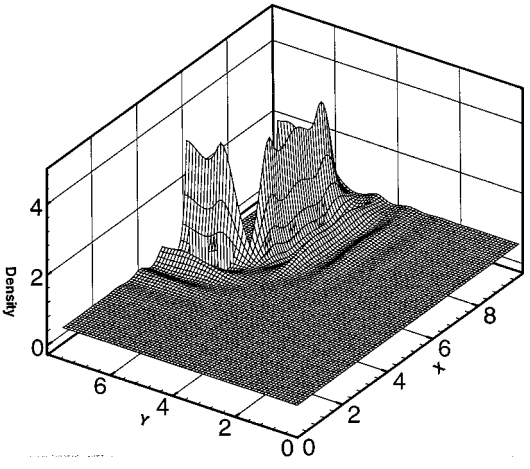

FIG. 3. The density ($\rho\sigma^3$) distribution in the solvation shell around two square rod polymers, where $\rho_b\sigma^3 = 0.65$ and $D/\sigma = 1.5$.

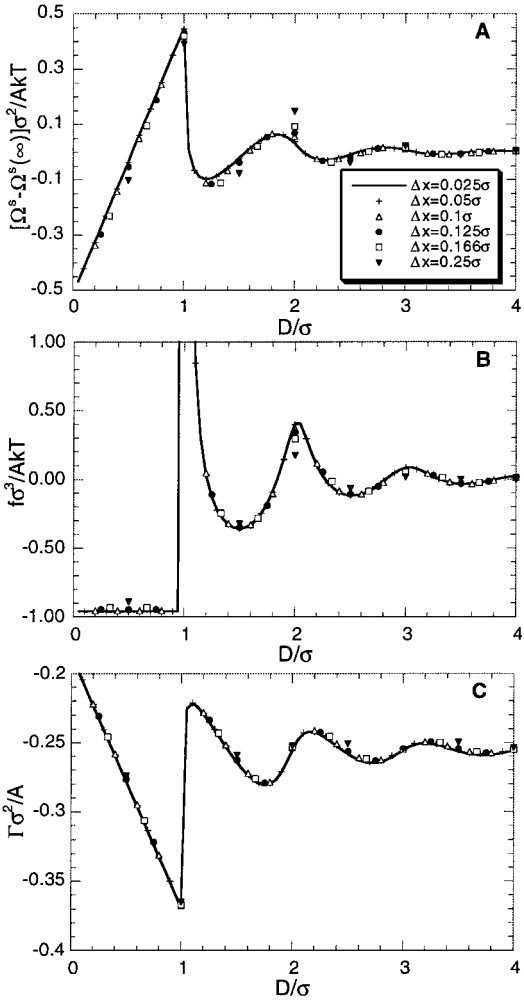

FIG. 4. (A) The shifted surface free energy per unit area, $[\Omega^s(D) - \Omega^s(\infty)]/A$, where $\Omega^s(\infty) \approx \Omega^s(6\sigma)$. (B) The x-component of the solvation force, $f \equiv f_s^x$, per unit area. (C) The excess adsorption per unit area. Each panel shows results for mesh densities ranging from $\Delta x = 0.025\sigma$ to $\Delta x = 0.25\sigma$, as indicated in the legend. The normalizing area is the total surface area (i.e., $A = 12\sigma \times L$) of one rod. The values of $\Omega^s(6\sigma)\sigma^2/AkT$ used for (A) were 1.87, 1.88, 1.92, 1.95, 2.01, and 2.15 for $\Delta x/\sigma = 0.025$, 0.05, 0.1, 0.125, 0.166, and 0.25, respectively.

molecular diameter. The solvation force in y is strictly zero due to symmetry and thus is not shown. The surface free energy is shifted by the infinite separation limit. When shifted, the surface free energy is equivalent to the potential of mean force acting between the rods [13, 14]. Thus the global minimum in Fig. 4A yields a prediction of the equilibrium separation of the polymer strands.

All of the parameters in Fig. 4 show oscillations of period σ that reflect solvent packing constraints near the surfaces. The discontinuity that arises at $D/\sigma = 1$ is the result of osmotic exclusion of solvent from the gap between the surfaces. Since our fluid is a hard sphere fluid, no fluid molecules will fit in the gap when it is smaller than 1σ in size.

It should be noted that the discontinuity at $D/\sigma = 1$ is a slope discontinuity for the free energy and adsorption while it is a value discontinuity for the force. As $D/\sigma \to 1$ from

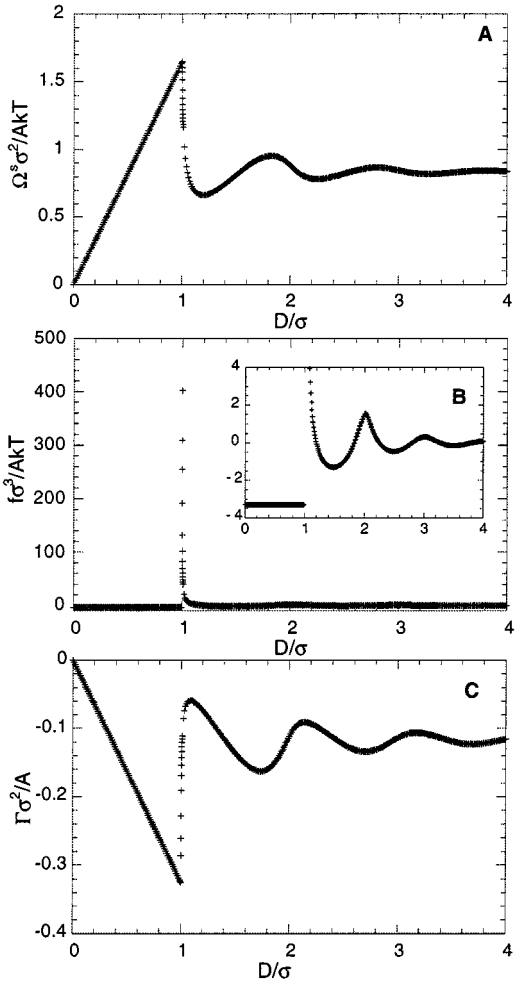

FIG. 5. (A) The surface free energy per unit area, Ω^s/A. (B) The x-component of the solvation force, $f \equiv f_s^x$. (C) The excess adsorption per unit area from 1D calculations of a hard sphere fluid confined between hard parallel planar surfaces.

above, there will be nonzero densities at the nodes $x = L_x$ and $y \geq L_y - 1.5\sigma$ (see Fig. 2). However, the density in the elements surrounding those nodes is strictly zero. Thus while these nonzero densities contribute to the surface integral that yields the force, they do not contribute to the volume integrals of the surface free energy and adsorption. This point is illustrated more precisely in Fig. 5, where the results of 1D calculations (based on mesh sizes as small as $\Delta x/\sigma = 0.00025$) of a fluid confined between smooth parallel planar surfaces are detailed.

There is good agreement among the results of all the mesh densities shown in Fig. 4. The largest errors are found at the peaks in the force curve ($D/\sigma = 1, 2, \ldots$), where f_s^x is underestimated and Ω^s is overestimated. The forces at $D/\sigma = 1$ are not shown in Fig. 4B. They are $f_s^x\sigma^3/AkT = 89.518$, 89.520, 89.490, 89.469, 89.429, and 89.208 for $\Delta x = 0.025$, 0.05, 0.1, 0.125, $0.16\overline{6}$, and 0.25.

A test of the force sum rule for $0.025 \leq \Delta x \leq 0.25$ can be found in Fig. 6. The partial derivative, $\partial\Omega^s/\partial D$, was estimated numerically with central finite differences around the

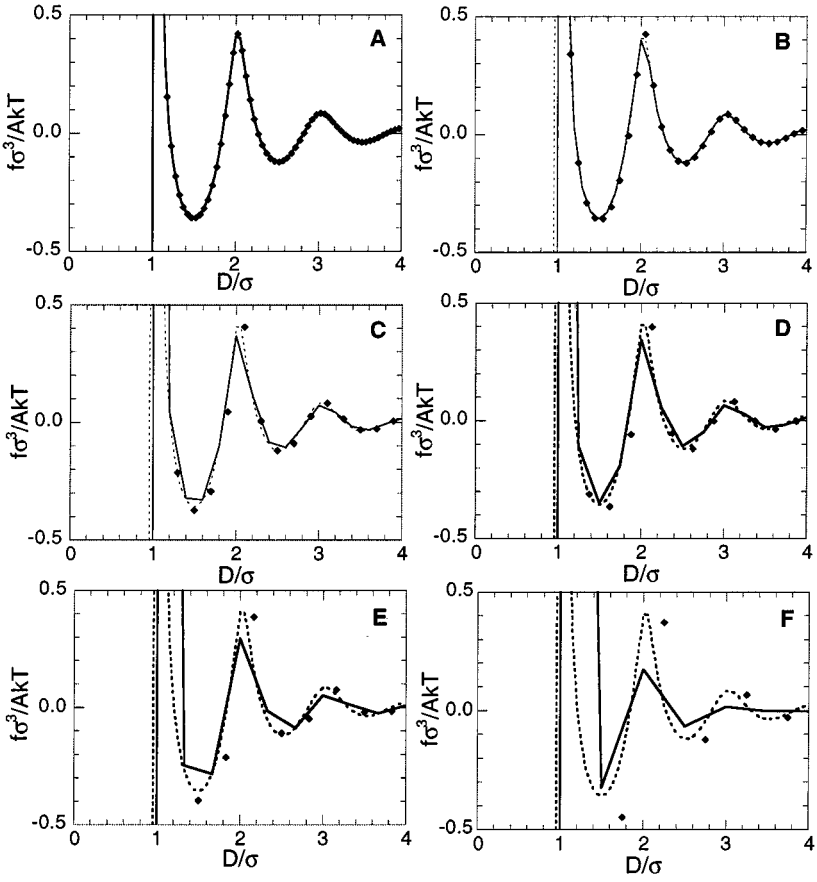

FIG. 6. A comparison of the two methods for calculating the force where the solid lines indicate $f_s = \int \rho(\mathbf{r}_s)\, d\mathbf{r}_s$ and the symbols indicate $f_s = -\partial\Omega^s/\partial D$. The mesh density in the zone nearest the surface varies with $\Delta x = 0.025$ (A), $\Delta x = 0.05$ (B), $\Delta x = 0.1$ (C), $\Delta x = 0.125$ (D), $\Delta x = 0.166$ (E), and $\Delta x = 0.25$ (F). The dotted line in (B)—(F) is the $\Delta x = 0.025$ result using $f_s = \int \rho(\mathbf{r}_s)\, d\mathbf{r}_s$.

points $D + 0.5\Delta D$, where $\Delta D = 2\Delta x$ is the spacing between points in Fig. 4. Figure 6 confirms that the free energy derivative in Eq. (5) gives a good estimate of the force in all cases except $\Delta x = 0.25\sigma$, where the spacing between successive data points ($\Delta D = 0.5\sigma$) is too large for accurate numerical derivatives.

4. CYLINDRICAL POLYMERS

We now turn to the cylindrical polymers where the geometry of the polymer surface changes as the mesh is refined. As was discussed in Part I, the surfaces in our calculations are defined by identifying each element in the solution domain as being either entirely in the fluid or entirely in one of the surfaces in the calculation. Since our mesh is Cartesian, the curved surfaces are staircased, and the surface geometry will depend on mesh spacing. Thus it is necessary to determine how sensitive the free energy, force, and adsorption predictions are to these geometry changes.

The calculations presented here are based on the computational domain of Fig. 2B. An example of the fluid density in one quadrant of the solvation shell around two interacting

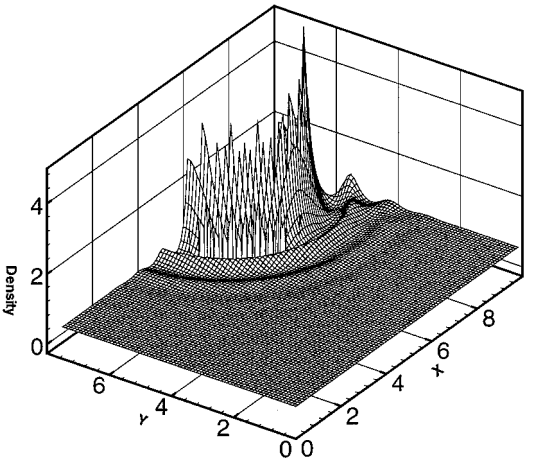

FIG. 7. The density ($\rho\sigma^3$) distribution in the solvation shell around two square rod polymers, where $\rho_b\sigma^3 = 0.65$ and the surface separation at the point of closest approach ($y = L_y$) is $D/\sigma = 1.5$.

cylinders is shown in Fig. 7. Note that the densities at the surface of the cylinder are now quite jagged due to the staircasing. Contrast this with the smooth density profiles at the surface of the square rod polymer in Fig. 3.

Figure 8 shows Ω^s, f_s, and Γ as a function of the surface separation of the cylinders. Again, all of these parameters have oscillations on the period of σ. However, the amplitudes of the oscillations in f_s and Ω^s are reduced in comparison with the square rods. This reduction in the solvation oscillations results from the surface curvature of the cylinder.

One striking feature of Fig. 8 is the jagged nature of the force when $D/\sigma \leq 1$. These jagged peaks have the same origin as the single discontinuity observed for the square rods. However, in the case of the cylinders, all separations $D/\sigma < 1$ can show the discontinuity because there is some element on the cylindrical surface that has a separation of exactly 1σ with the corresponding element on the opposing surface.

The slope discontinuities observed in Figs. 4B and 4C at $D/\sigma = 1$ are not obviously present in either the Ω^s or Γ curves in Figs. 8B and 8C. However, both of these parameters are more sensitive to mesh density than was observed for the square rods. For example, Γ is underestimated at $D/\sigma \approx 0.5$ while the Ω_s is overestimated at $D/\sigma \approx 0.8$ and 1.8 for the coarser meshes. In addition the Γ curves in Fig. 8C required shifting for clarity of presentation, as detailed in the figure caption.

Once again, the force sum rule was applied to test the self-consistency of the calculations. The free energy derivatives (see Eq. (5)) are shown in Fig. 9 for a variety of mesh spacings.

Unlike the direct calculation (Fig. 8B), the free energy derivatives are not jagged for $D/\sigma \leq 1$. Rather, all the different grids ($\Delta x \leq 0.16\overline{6}$) give surprisingly consistent results. Surface free energies on any of these grids may therefore be used to obtain an estimate of the force for an infinitely refined mesh. Clearly, the surface integral in Eq. (5) is more sensitive to geometry changes with mesh spacing than are the volume integrals that are used to calculate Ω^s.

Returning to the results in Fig. 8B, the magnitude of the jagged peaks at $D/\sigma \leq 1$ decreases as Δx decreases. In the limit $\Delta x \to 0$, we would expect these jagged peaks to disappear. One way to estimate this limit is to take the force to be the mean of $f_s(d/\sigma \to 1_+)$

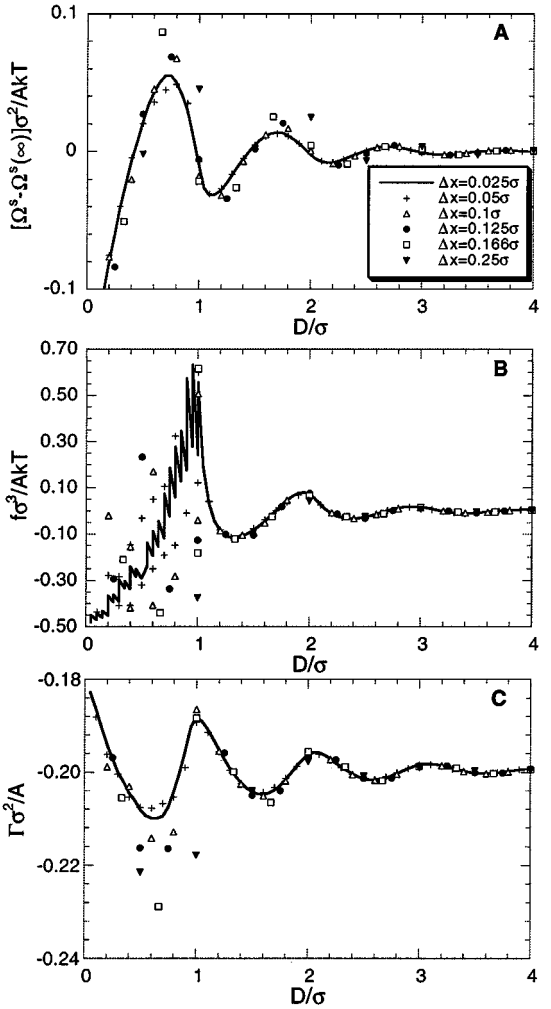

FIG. 8. Same as Fig. 4 except for cylindrical rods. The normalizing area is the total surface area of one cylinder (i.e., $A = 12\sigma \times L$). The values of $\Omega^s(6\sigma)\sigma^2/AkT$ used for (A) were 1.46, 1.46, 1.47, 1.61, 1.48, and 1.94 for $\Delta x/\sigma = 0.025$, 0.05, 0.1, 0.125, 0.16$\bar{6}$, and 0.25, respectively. The excess adsorptions, Γ, were all shifted to the limit of the $\Delta x = 0.025$ data for clarity of presentation. Before shifting, the limiting values of the adsorptions were $\Gamma\sigma^2/A = -0.197$, -0.191, -0.212, -0.171, and -0.223 for $\Delta x = 0.05$, 0.1, 0.125, 0.16$\bar{6}$, and 0.25.

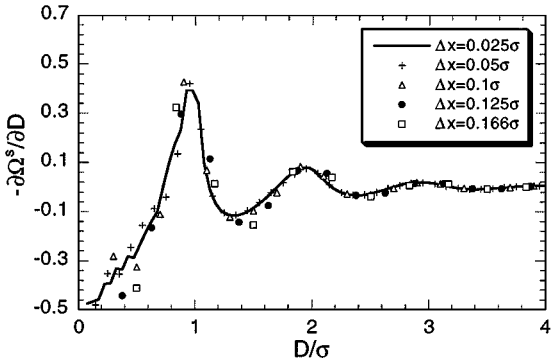

FIG. 9. A comparison of the solvation force, $f_s = -\partial\Omega^s/\partial D$, as a function of the surface separation D between parallel cylinders for a variety of grid spacings.

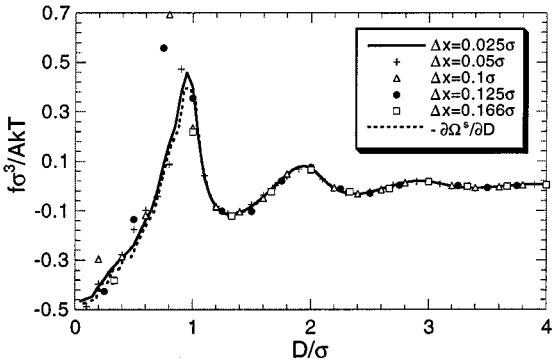

FIG. 10. The solvation force as function of the surface separation where the force is calculated with $f_s = \int \rho(\mathbf{r_s})\, d\mathbf{r_s}$, but for separations of $D/\sigma \leq 1$, the force is estimated with $f = 0.5 * [f_s(d/\sigma \to 1_+) + f_s(d/\sigma \to 1_-)]$.

and $f_s(d/\sigma \to 1_-)$, where d is the surface separation associated with each surface element. Mean force estimates for several mesh spacings are shown in Fig. 10. For $\Delta x/\sigma = 0.025$ and 0.05, there is good agreement between the mean force and the free energy derivative. For larger Δx, the maximum in the first peak is overestimated. However, in all cases, this estimate of the force is considerably closer to the infinitely refined mesh result than are the jagged forces in Fig. 8B.

5. BEAD–CHAIN POLYMERS

Finally, we consider the bead–chain polymers. For all the calculations presented below, the mesh spacing in the finest zone is taken to be $\Delta x = 0.125\sigma$. The computational domain in x includes two bead-chain polymer strands, as is sketched in Fig. 2C.

The bead–chain polymer model in Fig. 1 is qualitatively different from the square rods and cylindrical polymers in that it is nonuniform in the axial direction. Thus, the solvation structure is complex in 3D. Figures 11 and 12 show densities in the solvation shells surrounding two bead-chain polymers in the planes $z = 0$ and $z = L_z$ when the center to center separation is $H = 4.5\sigma$. The $z = 0$ slice corresponds the the point where two beads on a given chain meet and the surface separation is $D = H$. The $z = L_z$ slice is the z plane where the surface separation is smallest, $D = H - 3\sigma$. While the peak densities in the $z = L_x$ plane are comparable to square rod polymers and cylindrical polymers (see Figs. 3 and 7), the peak densities in the $z = 0$ plane are significantly higher.

The large densities in Fig. 11 arise from the large fluid–surface interactions that occur in the annulus around the point where two neighboring beads on a single chain meet. The fluids in these regions can be considered to be *bound* although they are not chemically bonded to the polymer.

The complexity in the solvation structure has a significant effect on f_s, Ω^s, and Γ, as shown in Fig. 13. While all the parameters show solvation oscillations, the amplitudes of the oscillations are reduced in comparison with both the parallel cylinders and square rods. Thus, the additional surface roughness is a destructive factor with respect to solvation forces. Surface roughness is a subtle issue that is beyond the scope of the current discussion; however, it has been shown that surface roughness may be either destructive (as in the present case) or constructive with respect to solvation forces between rough planar

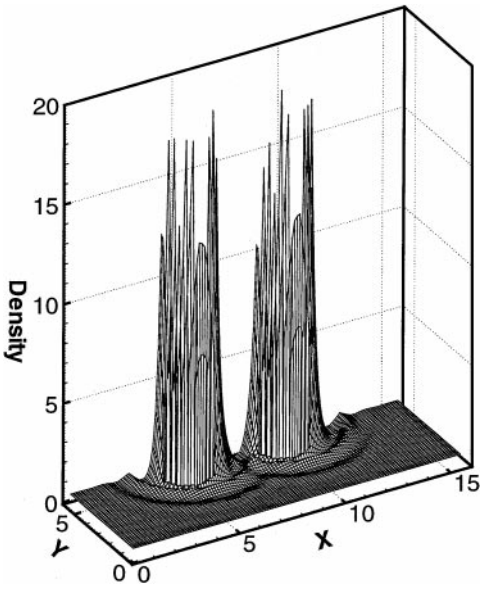

FIG. 11. A slice at $z = 0$ of the density ($\rho\sigma^3$) distribution in the solvation shell around two bead–chain polymers where $\rho_b\sigma^3 = 0.63$ and the center–center separation of the strands is $H/\sigma = 4.5$.

surfaces [15]. Thus one might obtain a different result if the size of the beads were increased or decreased.

It should be noted that we were not able to obtain a solution at $H/\sigma = 3.25\sigma$ for the bead–chain model. We observed that a numerical instability arises when the large densities found between neighboring beads on the same chain (at $z = 0$) begin to interact with a large density peak that occurs at the intersection of exclusion zones between the two polymer strands. The location of this peak is a new site for fluid *binding*.

Figures 14 and 15 show the development of *bound* fluid molecules in the chain–chain interaction region. In both cases, $y = 4.625\sigma$ slices of the density distribution are shown. In Fig. 14, the separation of the polymer strands is $H/\sigma = 4.5$ while in Fig. 15, it is $H/\sigma = 3.5$. In the former case, four density peaks may be observed in the $z = 0$ plane. These peaks represent fluid molecules bound in the bead–bead interaction annuli. In the latter case, there are five density peaks. The first four are again in the $z = 0$ plane, corresponding to

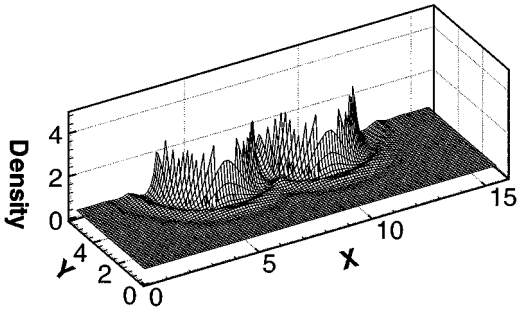

FIG. 12. A slice at $z = L_z$ of the density ($\rho\sigma^3$) distribution in the solvation shell around two bead–chain polymers, where $\rho_b\sigma^3 = 0.63$ and the center–center separation of the strands is $H/\sigma = 4.5$.

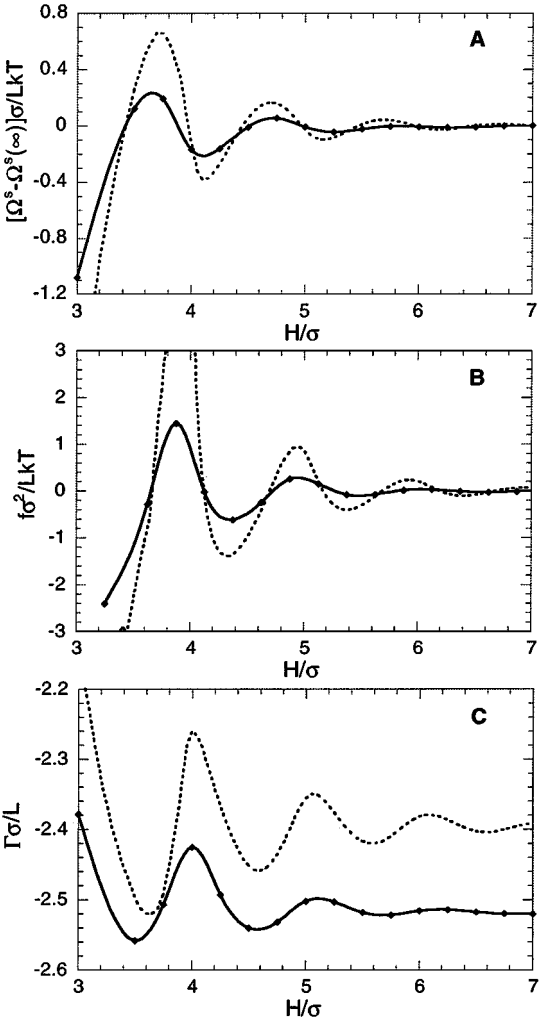

FIG. 13. Results for bead–chain polymers (solid lines) compared to cylindrical polymers (dashed lines). Variables are the same as in Fig. 4 but are given per unit length (L/σ) of the polymer chains. The infinite separation limit was taken to be $[\Omega^s(\infty) \approx \Omega^s(H = 7\sigma)]\sigma^2/AkT = 1.304$, and the mesh spacing is fixed at $\Delta x = 0.125$. The solvation forces shown as solid and dotted lines were calculated using $f_s = -\partial\Omega^s/\partial H$. The normalizing area for the bead–chain model (when $L = 1.5\sigma$) is $A = 20.5\sigma^2$.

bead–bead interaction annuli. The fifth peak is found at the narrowest point of the interaction region between the two chains. This fifth peak is of magnitude similar to that of the other four, indicating that fluid molecules in this region are bound as strongly as the fluid in the bead–bead interaction annuli.

When peaks 2, 3, and 5 are too close together, the unfavorable energy due to their interaction (corresponding physically to overlapping electron clouds) causes the observed numerical instability. The numerical instability arises physically from a local crystallization (or binding) of the fluid particles. Local crystallization is not well resolved by our current implementation because it is impossible for our direct solve on a fixed mesh grid using linear basis functions to capture the steep density profiles that must approach delta functions. The problem may also be exacerbated in our calculations by the application of Rosenfeld's

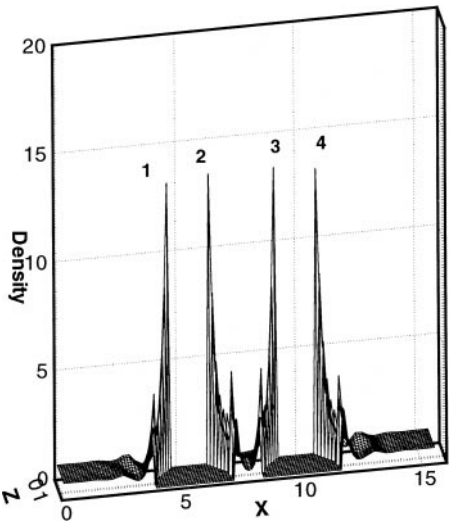

FIG. 14. An example of one slice (at $y = 4.625\sigma$) of the density distribution in a hard sphere fluid near two hard bead–chain polymers. The bulk fluid density is $\rho\sigma^3 = 0.63$, and the center–center separation of the chains is $H = 4.5\sigma$.

original functional, which is known to exhibit incorrect zero-dimensional crossover behavior [16]. Due to numerical limitations, a Gaussian basis approach [17] may be needed for cases where strong solvent localization is important.

Finally, we note that for all of the polymer models considered here, the osmotic exclusion effect dominates with respect to self-assembly. Osmotic exclusion is maximized when the surfaces are in contact with one another. Since the global free energy minimum is found, in all cases, at the point of contact, it can be concluded that at equilibrium all of these model

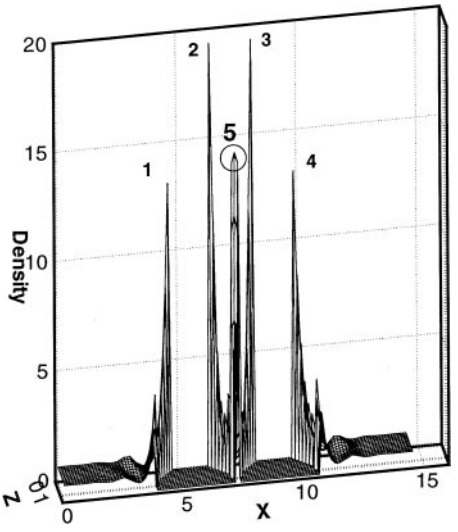

FIG. 15. An example of one slice (at $y = 4.625\sigma$) of the density distribution in a hard sphere fluid near two hard–chain polymers. The bulk fluid density is $\rho\sigma^3 = 0.63$, and the center–center separation of the chains is $H = 3.5\sigma$.

polymers would assemble in a hard sphere solvent with the minimum number of solvent molecules between the polymer strands. Since the free energies of the interactions are given per unit length (in units of σ) of the strand, the height of the free energy barriers (as well as the depths of the wells) will ultimately be determined by the length of the chain.

6. SUMMARY

In this paper, we detailed the precision of a novel 2D and 3D nonlocal DFT code. We applied this code to several polymer models in order to separate the effect of mesh spacing on precision from the effect of mesh spacing on surface geometry. Using 2D models, we showed that acceptable results (forces, free energies, adsorptions) can be obtained for mesh spacings $\Delta x \leq 0.16\overline{6}\sigma$.

We also have explored the effect of polymer geometry on the magnitude of solvation forces. In all cases oscillatory solvation forces were found. However, the addition of surface curvature and roughness were found to decrease the magnitude of the oscillations. Calculations for the 3D bead–chain polymer model showed how the presence and location of *bound* fluid molecules can be identified with this nonlocal DFT code. We found that in the bead–chain model fluid atoms are always bound in the annuli around the points where two beads on one chain meet. In addition, when two beads are close together, bound fluid molecules are found in the interaction region between the polymer strands. At certain separations, solutions could not be obtained apparently due to unfavorable interactions of the bound molecules. Molecular simulations are needed to understand the physical significance of these numerical instabilities.

The results in this paper serve to demonstrate the power of this 2D/3D DFT code for predicting the structure of solvation shells and the associated solvation forces, surface free energies, and adsorptions in complex geometries. These calculations may be used to assess the qualitative and quantitative differences between models (e.g., bead–chain vs cylindrical polymers). They may also be used to estimate the importance of solvent structural forces in comparison with other physical forces (e.g., electrostatic forces). Finally, the code may be easily extended to complex surfaces ranging from biological macromolecules (e.g., proteins) to porous materials (e.g., zeolites). Thus the DFT may be used in conjunction with more traditional molecular simulations to elucidate the properties of solvated systems.

ACKNOWLEDGMENTS

Sandia is a multiprogram laboratory operated by Sandia Corporation, a Lockheed Martin Company, for the United States Department of Energy under Contract DE-AC04-94AL85000.

REFERENCES

1. T. K. Vanderlick, L. E. Scriven, and H. T. Davis, Molecular theories of confined fluids, *J. Chem. Phys.* **90**, 2422 (1989).
2. I. K. Snook and W. van Megen, Solvation forces in simple dense fluids, 1, *J. Chem. Phys.* **72**, 2907 (1980).
3. L. J. Douglas Frink and F. van Swol, A molecular theory for surface forces adhesion measurements, *J. Chem. Phys.* **106**, 3782 (1997).
4. E. Velasco and P. Tarazona, Prewetting at a solid–fluid interface via Monte-Carlo simulation: Comment, *Phys. Rev. A* **42**, 2454 (1990).

5. L. J. Douglas Frink and A. G. Salinger, Wetting of a chemically heterogeneous surface, *J. Chem. Phys.* **110**, 5969 (1999).
6. J. R. Henderson, Statistical mechanics of patterned inhomogeneous fluid phenomena, *J. Phys. Condens. Matter* **11**, 629 (1999).
7. L. J. Douglas Frink and F. van Swol, Stress isotherms of porous thin materials: Theoretical predictions from a nonlocal density functional theory, *Langmuir* **15**, 3296 (1999).
8. L. J. Douglas Frink and A. G. Salinger, Two- and three-dimensional nonlocal density functional theory for inhomogeneous fluids. I. Algorithms and parallelization, *J. Comput. Phys.* **159**, 407 (2000).
9. D. Henderson, Ed., *Fundamentals of Inhomogeneous Fluids* (Dekker, New York, 1992).
10. Y. Rosenfeld, Free-energy model for the inhomogeneous hard-sphere fluid mixture and density-functional theory of freezing, *Phys. Rev. Lett.* **63**, 980 (1989).
11. S. A. Allison and S. Mazur, Modeling the free solution electrophoretic mobility of short DNA fragments, *Biopolymers* **46**, 359 (1998).
12. N. Jensen, R. J. Mashl, R. F. Bruinsma, and W. M. Gelbart, Couterion-induced attraction between rigid polyelectrolytes, *Phys. Rev. Lett.* **78**, 2477 (1997).
13. L. J. Douglas Frink and F. van Swol, Solvation forces and colloidal stability: A combined Monte-Carlo and density-functional theory approach, *J. Chem. Phys.* **100**, 9106 (1994).
14. T. L. Hill, *Statistical Mechanics* (McGraw–Hill, New York, 1958).
15. L. J. Douglas Frink and F. van Swol, A molecular theory for surface forces adhesion measurements, *J. Chem. Phys.* **106**, 3782 (1997); Solvation forces between rough surfaces, *J. Chem. Phys.* **108**, 5588 (1998).
16. Y. Rosenfeld, M. Schmidt, H. Löwen, and P. Tarazona, Dimensional crossover and the freezing transition in density-functional theory, *J. Phys. Condens. Matter* **8**, L577 (1996).
17. R. Ohnesorge, H. Löwen, and H. Wagner, Density-functional theory of crystal fluid interfaces and surface melting, *Phys. Rev. E* **50**, 4801 (1994).